MMS observations of energized He^+ pickup ions at quasi-perpendicular shocks

M. J. Starkey[1,2], S. A. Fuselier[2,1], M. I. Desai[2,1], S. J. Schwartz[3], C. T. Russell[4], H. Wei[4], H. Madanian[2], J. Mukherjee[2], L. B. Wilson III[5]

Abstract

Accelerated He^+ PUIs, downstream of quasi-perpendicular shocks, are studied as a function of the fast mode Mach number (M_f) and shock obliquity (θ_{Bn}). We analyze 10 quasi-perpendicular shocks with Mach numbers in the range [1, 7] observed by the Magnetospheric MultiScale (MMS) mission, and compare upstream and downstream He^+ velocity distribution functions (VDFs). For each shock event, we characterize the upstream PUI distribution and derive reduced 1D velocity distributions for the selected upstream and downstream intervals. We also compare the upstream to downstream ratio of spectral indices, computed from the He^+ perpendicular distributions, to M_f and θ_{Bn}. We find a positive correlation between this spectral index ratio and M_f, which suggests that perpendicular energization of He^+ PUIs is enhanced as the shock becomes stronger. These results inform modeling efforts of PUIs and shock acceleration processes, particularly those taking place at the termination shock.

Corresponding author michael.starkey@contractor.swri.org
[1]Physics and Astronomy, University of Texas at San Antonio, San Antonio, TX, USA
[2]Southwest Research Institute, San Antonio, TX, USA
[3]Laboratory for Atmospheric and Space Physics, University of Colorado Boulder, Boulder, CO, USA
[4]Earth, Planetary, and Space Sciences, University of California, Los Angeles, CA, USA
[5]NASA Goddard Space Flight Center, Greenbelt, MD, USA

1. Introduction

Collisionless shocks are a ubiquitous phenomenon that occur naturally in space plasma environments. They are characterized by sharp discontinuities in the local magnetic field, bulk plasma density, and bulk flow speed. They mediate the transition between supersonic and subsonic plasma flows. Typically, shocks are classified by the angle (θ_{Bn}) between the upstream magnetic field and the shock normal vector ($\vec{n}_{sh}$), which points into the upstream region. When $\theta_{Bn} < 45°$, the shock is referred to as quasi-parallel, whereas shocks with $\theta_{Bn} > 45°$ are referred to as quasi-perpendicular. The strength of the shock is typically characterized by the Alfvenic Mach number ($M_A = \frac{v_{up}^n}{v_A}$), or the fast mode Mach number ($M_f = \frac{v_{up}^n}{v_f}$). Here, v_{up}^n is the upstream bulk plasma flow speed normal to the shock surface, v_A is the Alfven flow speed, and v_f is the speed of the fast mode magnetosonic wave. These Mach numbers, along with the shock angle, are useful parameters for the systematic study of ion dynamics at shocks.

Within the heliosphere, shocks are categorized into two types: traveling and stationary shocks. Within each category exists multiple subclasses, resulting in a rich variety of shocks present throughout the heliosphere. Traveling shocks refer to those that move through interplanetary space, relative to the Sun, such as coronal mass ejection (CME)-driven interplanetary shocks (e.g., Desai et al., 2004) or forward/reverse shocks bounding corotating interaction regions (CIR) within the solar wind (SW; e.g., Mason et al., 2008). On the other hand, stationary shocks are those that do not move much with respect to the Sun, such as planetary bow shocks (e.g., Desai et al., 2000) and the termination shock which is one of the boundaries in the outer heliosphere (e.g., Stone et al., 2005). Such variety results in complex interactions between shocks and local particle populations. Indeed, it is understood that collisionless shocks are important generators of energetic particle populations throughout the heliosphere (e.g., Lee, 1983; Jones & Ellison, 1991; Desai & Burgess, 2008).

The leading theory for ion acceleration at shocks is diffusive shock acceleration (DSA; Fisk & Lee, 1980; Lee, 1983, Jones & Ellison, 1991). Encompassed within this theory are two main mechanisms which are thought to accelerate ions: the first order Fermi mechanism (Baring, 1997; Caprioli et al., 2010) and the shock drift acceleration mechanism (SDA; Chen & Armstrong, 1975; Decker, 1981, 1983; Caprioli et al., 2015). For a time, SDA was thought to be separate altogether from DSA. However, as discussed in Jones & Ellison (1991), work by Kota (1979) and Jokipi (1979, 1982) has shown that the energy gain due to curvature and gradient drifts is included in the diffusion-convection equation of DSA (see Jones (1990) for a derivation). While the Fermi mechanism is more efficient for high-energy particles (> ~10s of keV), SDA is capable of accelerating thermal and suprathermal particles (Caprioli et al., 2015). Furthermore, both processes act simultaneously at a shock, however the relative importance of each is thought to depend on the shock geometry (θ_{Bn}; Jones & Ellison, 1991; Jokipii, 1982; Decker & Vlahos, 1986). At quasi-parallel shocks, particles are able to diffuse back and forth across the shock via collisions with magnetic obstacles. Due to the differences in the upstream and downstream bulk motion of these obstacles, the diffusing particles experience a net increase in momentum. This Fermi mechanism is thus thought to be more efficient at quasi-parallel shocks. On the other hand, at quasi-perpendicular shocks, SDA is expected to be the dominant mechanism responsible for particle acceleration. In SDA theory, ions are reflected by the magnetic gradient at the shock, and resample the shock multiple times due to their gyration about the local magnetic field. Upon each interaction with the shock, the ion feels the force of the upstream solar wind (SW) electric field $\left(\vec{E}_{SW} = -\vec{v}_{SW} \times \vec{B}_{IMF}\right)$ and is accelerated through the upstream region.

Eventually the ion is able to escape downstream of the shock with a net increase in energy. There are other mechanisms which can also play significant roles in ion acceleration at quasi-perpendicular shocks: specular shock reflection (SR; Sonnerup, 1969; Sckopke et al., 1983, 1990; Sckopke, 1995), shock surfing (SS; Lee et al., 1996), and multiply reflected ion acceleration (MRI; Zank et al., 1996). In particular, SR, in which an incident ion is reflected by the cross-shock electrostatic potential, has been shown to play a significant role in ion acceleration at near perpendicular shocks (Oka et al., 2002b; Starkey et al., 2019). While the process by which an ion resamples the shock is different for each of the mentioned mechanisms, the energy gain for each is due to drift or gyratory motion through the upstream electric field. For instance, an ion that is specularly reflected at a quasi-perpendicular shock will gyrate through the upstream electric field, resulting in a net energy gain once the ion escapes downstream. Thus, at quasi-perpendicular shocks, ions are expected to be accelerated largely in a direction perpendicular to the magnetic field, rather than parallel to the field.

In this paper we study quasi-perpendicular shocks and how ion acceleration at these shocks changes with shock parameters. To date, ion acceleration at Earth's high Mach perpendicular bow shock has been studied extensively through observations and modeling (Paschmann et al., 1980; Sckopke, 1995; Sckopke & Paschmann, 1983; Sckopke et al., 1990; Sonnerup, 1969; Burgess et al., 2012). The effect of Mach number and θ_{Bn}, regarding the degree to which ions are accelerated, has also been studied in simulations (Leroy et al., 1981, 1982). The general consensus is that the acceleration efficiency should increase with Mach number and that these effects are largely perpendicular to the magnetic field. However, it is not fully understood how these acceleration processes act on distinct ion populations within the solar wind. For example, mechanisms such as SDA and SR require ions with specific velocity space characteristics in order to be efficient. Thus, these mechanisms may act differently on ion populations with different velocity characteristics, such as the interstellar pickup ions, from those of the bulk solar wind.

Interstellar pickup ions (PUI) are interstellar neutral particles that have become ionized in transit through the heliosphere. Upon ionization, a freshly born PUI moves with speed $|\vec{v}_{SW} - \vec{v}_{LISM}|$ relative to the solar wind, where $\vec{v}_{LISM}$ is the velocity of neutral particle population within the local interstellar medium (LISM) from which the fresh PUI was born. This motion consists of a guiding center motion and a gyromotion around the local interplanetary magnetic field (IMF). The gyrospeed is $\leq v_{SW} + v_{LISM}$ in the plasma frame and depends on the direction of the SW flow and the IMF. Thus, fresh PUI velocity distribution functions (VDF) will resemble a ring in the SW reference frame, whose axis is aligned with the IMF direction. In the rest frame of the Sun, or a slowly moving spacecraft, the velocity boundary of this ring will have a maximum possible speed of $2 * |\vec{v}_{SW} - \vec{v}_{LISM}|$. This maximum cutoff speed has typically been used to identify high energy PUIs in SW ion distributions (Zirnstein et al., 2018; Zank et. al., 1996). Furthermore, due to their generation mechanism, PUIs are distinguishable from bulk SW ions by their energy and velocity space characteristics (Möbius & Hovestadt, 1985; Gloeckler & Geiss, 1998; Gloeckler et al., 2004b; Drews et al., 2013, 2015; McComas et al., 2017; Gomez et al., 2019; Starkey et al., 2019, 2020). Not only are PUIs distinguishable from SW ions, but their velocity space characteristics make them ideal candidates for participation in the drift acceleration mechanisms discussed above. Indeed, recent theoretical and simulation work has suggested that due to their generation mechanism, singly charged PUIs form a possible source for shock-accelerated energetic particle populations observed throughout the heliosphere (Giacalone & Jokipii, 1995; Kucharek &scholar, 1995; Lee et al., 1996; Zank et al., 1996; Ellison et al., 1999; Yang et al., 2011). This suggestion has been confirmed through multiple observations of PUIs at quasi-perpendicular shocks (Gloeckler et al., 1994; Oka et al., 2002; Gloeckler et al., 2004a; Giacalone & Decker, 2010; Zirnstein et al., 2018; Starkey et al., 2019, 2020).

While interstellar H^+ is certainly the most abundant PUI within the SW, it is also convolved with SW and suprathermal H^+ and thus difficult to distinguish observationally. On the other hand, during quiet solar wind conditions, He^+ in the solar wind is typically of interstellar origin (Möbius & Hovestadt, 1985). Furthermore, due to the Sun's gravitational focusing of neutral Helium, the He^+ PUI density is increased within what is referred to as the Helium focus cone (Möbius & Hovestadt, 1985). As the Earth orbits the sun and passes through this focus cone, the higher density of He^+ PUIs enables better observations of these ions. Thus, He^+ PUIs form a suprathermal seed population in the solar wind that is distinguishable from SW thermal ions and readily observable, particularly when Earth is within the focus cone (Swaczyna et al., 2019). Since the Earth's bow shock is mediated by the bulk SW H^+, He^+ acts as a test particle at the shock and thus can be used as tracers of acceleration processes taking place at the shock. This characteristic makes He^+ a natural test particle species for the study of ion acceleration at quasi-perpendicular shocks.

Understanding how PUIs are accelerated at quasi-perpendicular shocks informs modeling of PUIs throughout the heliosphere. In particular, it provides insight into the physics surrounding the heliospheric termination shock. As the solar wind moves radially outward from the Sun, the relative density of PUIs increase. In the outer heliosphere, PUIs begin to dominate the SW dynamic pressure. Thus, PUIs are thought to heavily influence the termination shock, which is considered a quasi-perpendicular shock (Zank et al., 1996). By studying how PUIs are accelerated at Earth's bow shock as a function of Mach number and θ_{Bn}, valuable insights are obtained into the ion dynamics at the termination shock. This in turn aids in the understanding of anomalous cosmic rays (ACRs), which are thought to be accelerated at the termination shock.

In this paper we study MMS observations of 10 quasi-perpendicular shocks (nine terrestrial bow shock crossings and one interplanetary shock) with varying Mach number and θ_{Bn}. We compare He^+ ion VDFs upstream and downstream of the shock and relative to the local magnetic field in order to identify signs of preferential ion heating or energization. We sample the parameter space defined by $M_f \in [1,7]$ and $\theta_{Bn} > 60°$. We also investigate changes in the power-law index of VDFs in the direction perpendicular to the magnetic field. These results help to explain how suprathermal He^+ populations interact with shocks of varying strength and geometry. Furthermore, this work informs future modelling and simulation efforts of PUI distributions and shock acceleration processes.

2. Spacecraft and Event Selection

We use ion distributions measured by the Hot Plasma Composition Analyzer (HPCA; Young et al., 2014), magnetic field data from the Fluxgate Magnetometer (FGM; Russell et al., 2016), and bulk SW velocity and density measurements provided by the Fast Plasma Investigation (FPI; Pollock et al., 2016) located on each of the four MMS spacecraft. We also use ion and electron temperature measurements provided by the Solar Wind Experiment located on the Wind spacecraft (Ogilvie et al., 1995) in our calculations of the M_f.

We first compiled a list of shocks (see Table 1) observed by MMS to include in this study, based on a set of selection criteria ($M_{ms} > 1$ and $\theta_{Bn} > 60°$). We limited our search window to the months of November – January during the years 2015-2019, which corresponded to dayside sweeps of the MMS spacecraft. We also chose these months so that the Earth and MMS were within the annual Helium focus cone, thus boosting He^+ measurement statistics. We identified shocks by sharp discontinuities in the magnetic field and bulk flow velocity. Most of the shocks that we identified were Earth's bow shock. However, in an effort to identify interplanetary shocks as well, we cross referenced the ACE list of interplanetary shocks with times when MMS was in the SW. We were only able to identify one interplanetary shock that was observed in the MMS data that conformed to our selection criteria. We next calculated the shock parameters for each shock and compared them to our selection criteria. For each of the bow shock observations, we calculated the shock normal and shock speed using ACE data as input to the Merka2005 model of Earth's bow shock (Merka et al., 2005). We also calculated the shock normal and shock speed using the magnetic coplanarity theorem. By comparing the two resulting vectors with the location of MMS at the time of the observation, we determined which normal vector and speed was more likely to represent the true shock parameters. Once the shock normal and shock speed was determined, we calculated the shock angle, θ_{Bn}, and the fast mode and Alfvenic Mach numbers, M_f and M_A, respectively. In these calculations, we used a 10-20 min averaging window directly upstream of the shock, which depended on how constant the upstream parameters were. Due to the inability of FPI and HPCA to resolve the solar wind beam, the resulting density and temperature measurements are somewhat underestimated. Thus, we use Wind data to estimate the upstream density and ion and electron temperatures, used in the calculations of M_f and M_A.

Table 1 lists the shocks that we included in this study based on this selection criteria. There are 9 bow shocks (labelled BS in the Type column) and one interplanetary shock, which was the forward shock of a CIR (labelled F-CIR). The last column shows the classification results of the upstream 2D distribution for each shock (see Section 4.1). The shock parameters for the Jan. 08, 2018 (S2) were taken from Cohen et al., 2019 which provided an in-depth analysis of this shock using burst data from MMS. The shocks are organized by increasing M_f. The last column shows the results of our classifications of each upstream 2D distribution (see Section 4.1). Table 1 also provides estimates of the magnetic and density compression ratios, computed using FGM and FPI (when available) data, respectively. The magnetic compression ratio was calculated using the transverse component of the magnetic field relative to each shock. Here, B_{up} and n_{up} are the upstream magnetic field strength and ion density, while B_{dn} and n_{dn} are the downstream quantities, respectively. These quantities were averaged over ~20 min intervals that started/ended ~2 min after/before the shock observation time. Note that three events (S8, S9, and S10) have magnetic compression ratios > 4, which conflicts with ideal MHD jump conditions. This may be due to a number of reasons: 1) contribution of relativistic particles to the shock mediation process, 2) time-dependent changes in the plasma that occur between measurements of upstream and downstream regions, and/or 3) issues with the underlying assumptions of ideal MHD. The error in each quantity shown was calculated by propagating the standard deviation of each measurement used in the calculation of that quantity. The shock angle relied heavily on the use of the Merka2005 model of Earth's bow shock, and so it is quite difficult to determine the error in each value of θ_{Bn}. Instead, an error of 5° was assigned to each value of θ_{Bn}, which was based on typical values for quasi-perpendicular shocks (Gonzalez-Esparza & Balogh, 2000). Our parameter space coverage includes M_f within the range $\sim[1,7]$ and θ_{Bn} within the range $\sim[60°,90°]$.

Shock Label	Shock Date	Shock Time (UT)	Type	θ_{Bn} (°)	M_A	M_f	B_{dn}/B_{up}	n_{dn}/n_{up}	Distribution Type (Upstream)
S1	2019-11-02	18:48	BS	$115/65 \pm 5$	2.7 ± 1.4	1.4 ± 0.7	3.8 ± 0.8	3.5 ± 4.3	Partial Shell
S2	2018-01-08	06:40	F-CIR	$113/67 \pm 5$	2.8 ± 1.3	1.9 ± 0.9	2.5 ± 0.1	2.2 ± 1.1	Ring
S3	2019-11-03	07:58	BS	$95/85 \pm 5$	2.8 ± 1.3	3.1 ± 1.0	4.1 ± 0.8	5.5 ± 4.7	Partial Shell
S4	2019-12-24	22:45	BS	$100/80 \pm 5$	5.3 ± 2.5	3.8 ± 1.8	3.7 ± 0.2	6.1 ± 1.7	Undetermined
S5	2019-11-11	10:10	BS	66 ± 5	5.5 ± 3.7	4.1 ± 2.2	3.2 ± 0.4	2.5 ± 5.9	Partial Shell
S6	2016-12-06	11:18	BS	$92/88 \pm 5$	5.7 ± 2.7	4.4 ± 2.0	4.0 ± 0.4	5.5 ± 7.9	Shell
S7	2019-11-16	12:52	BS	67 ± 5	9.2 ± 4.3	5.0 ± 2.4	2.6 ± 0.5	3.0 ± 2.9	Shell
S8	2016-12-06	12:04	BS	89 ± 5	8.4 ± 4.0	5.7 ± 2.5	5.0 ± 0.4	3.8 ± 5.1	Shell
S9	2015-11-20	06:51	BS	$92/88 \pm 5$	7.8 ± 3.7	5.9 ± 2.6	7.1 ± 0.7	2.9 ± 2.9	Ring
S10	2015-12-05	08:44	BS	85 ± 5	9.5 ± 4.5	6.1 ± 2.7	5.2 ± 0.8	3.9 ± 1.2	Shell

Table 1. List of shock events included in this study along with the calculated shock parameters and compression ratios. In the fourth column, BS indicates a bow shock observation while F-CIR indicates the forward shock of a CIR. The last columm shows the results of our classifications of the upstream 2D distributions (see Section 4.1). B_{up} and n_{up} are the upstream magnetic field strength and ion density, while B_{dn} and n_{dn} are the downstream quantities. The magnetic compression ratio was calculated using the transverse components of the magnetic field relative to the shock. The uncertainties shown are the propagated errors in each measurement, due to the temporal averaging of each quantity used in the calculation.

Figure 1 shows a quasi-perpendicular shock that was observed on Dec. 24, 2019 (S4) by MMS3. Panels a) and b) show the H^+ and He^+ omni-directional differential intensity measured by HPCA, respectively, followed by the FGM magnetic field strength in panel c) and the FPI ion (red) and electron (black) density in panel d). The last panel shows a comparison of the x-component of the HPCA bulk velocity (blue) and the FPI bulk velocity (black) in GSE coordinates. HPCA underestimates the bulk velocity when measuring the solar wind, as seen in panel d). Thus, when available, we use the FPI measured SW speed in this work. This particular shock was observed by MMS at 22:45 UT, and is identified by the sharp decrease in magnetic field strength accompanied by a sharp decrease in ion/electron density and a sharp increase in flow speed. The high H^+ flux to the left of the shock indicates that the MMS spacecraft was initially within the Earth's magnetosheath as the shock moved earthward across the spacecraft. To the right of the shock, the high flow speed (panel e), weak and constant field strength (panel c) and cold H^+ flux (panel a) indicates that MMS had entered the solar wind. Our next step was to analyze He^+ velocity distribution functions upstream/downstream of each of the 10 shocks listed in Table 1.

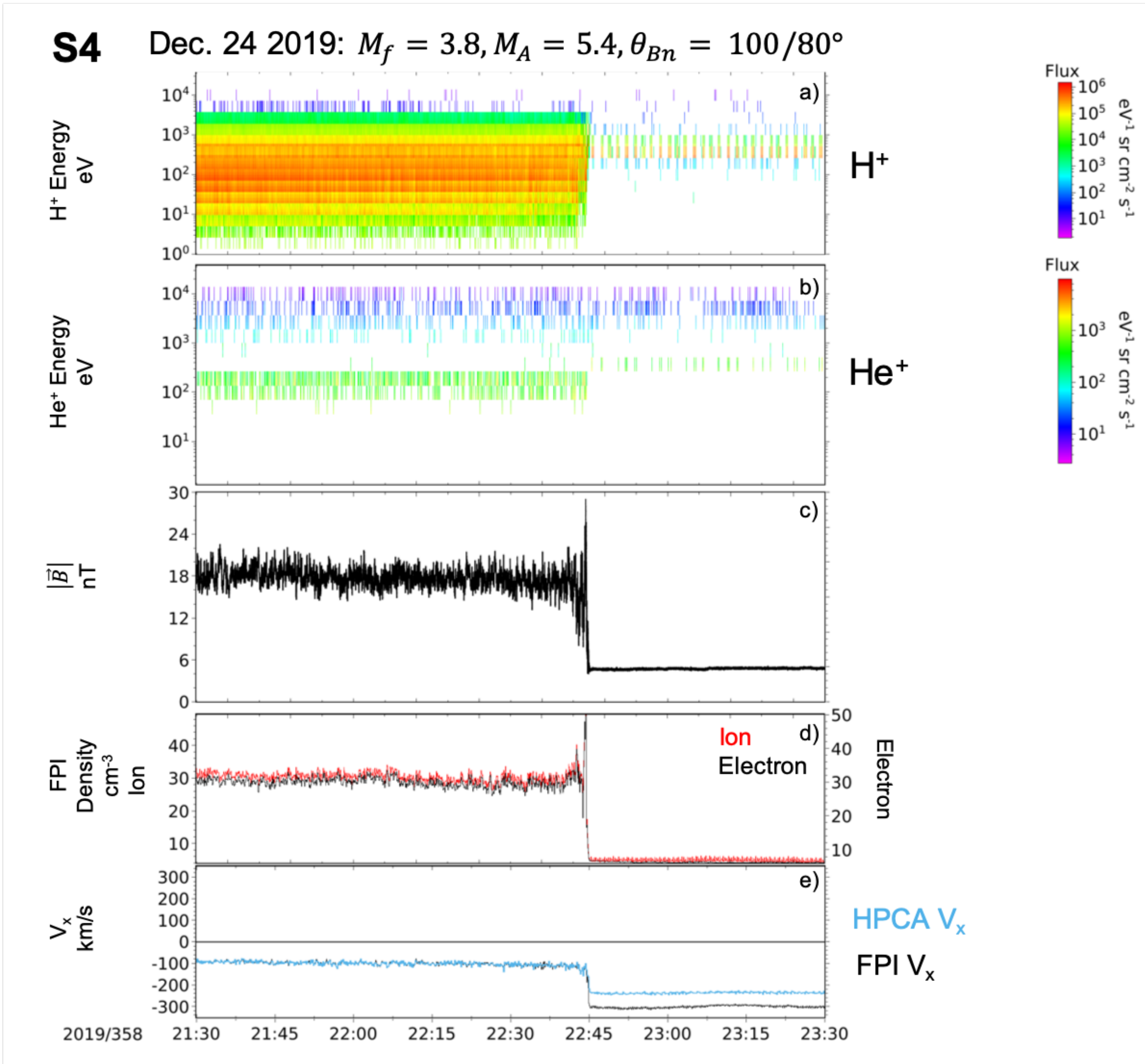

Figure 1. Overview of the bow shock event S4, observed by MMS3. Panels a) and b) show the H^+ and He^+ omni-directional differential intensity. Panels c) and d) show the FGM magnetic field strength and FPI measured ion and electron density. The last panel (f) shows the HPCA V_x component (blue) and FPI V_x component (black) of the bulk plasma velocity in GSE. The shock parameters calculated for this event are shown at the top of the plot. The shock is identified by the sharp discontinuities in field strength, density, and velocity, observed at ~22:45 UT.

3. Data Analysis

The He^+ distributions shown in this paper were measured by HPCA. HPCA is a toroidal electrostatic analyzer (ESA) optically coupled to a carbon foil time-of-flight (TOF) section and it provides measurements of an ion's energy-per-charge (E/Q) and mass-per-charge (M/Q) ratio, respectively (Young et. al., 2014). HPCA produces full 3D velocity distributions for each of the five ion species H^+, He^{2+}, He^+, O^{2+}, and O^+. In survey mode, HPCA scans through 63 E/Q steps, 16 azimuth look directions, and 16 elevations, which composes the full phase space of E/Q and solid angle (63 energy x 16 azimuth x 16 elevation) every 10 s. Each phase-space pixel is then assigned a velocity vector determined from the E/Q and look direction corresponding to that pixel. These velocity vectors then represent a 3D velocity distribution function (VDF) in geocentric solar ecliptic (GSE) coordinates, which correspond to the measured phase-space density (PSD).

3.1 Constructing 2D and 1D VDFs

For each shock analyzed in this paper, we identified intervals upstream and downstream of the shock over which ion distributions were averaged. We aimed to select long time intervals (on the order of 30 minutes), in order to boost He^+ statistics, over which the ion parameters were mostly stable. Once the upstream and downstream intervals were determined, we next translated the 3D VDFs from the spacecraft frame to the bulk plasma frame (determined from HPCA ion moments), and then rotated the distributions from GSE to a field aligned coordinate system defined by

$$\hat{x} = \frac{(\hat{b}\times\vec{V}_{Bulk})\times\hat{b}}{\|(\hat{b}\times\vec{V}_{Bulk})\times\hat{b}\|} \qquad \hat{y} = \frac{(\hat{b}\times\vec{V}_{Bulk})}{\|(\hat{b}\times\vec{V}_{Bulk})\|} \qquad \hat{z} = \hat{b} = \frac{\vec{B}_{IMF,GSE}}{\|\vec{B}_{IMF,GSE}\|} \;. \tag{1}$$

This was done for each velocity vector from the 3D VDF, using HPCA plasma moments and 10-sec averaged FGM magnetic field data. We next calculated 2D distributions from the 3D VDFs by averaging the VDFs around the gyrophase (φ), i.e., the local magnetic field direction:

$$f(V_\parallel, V_\perp) = \frac{1}{2\pi}\int_0^{2\pi} f(V_\perp, \varphi, V_\parallel)\, d\varphi\,. \tag{2}$$

We first defined a uniformly spaced Cartesian grid of velocities (40 x 40 km/s bins) of $V_\parallel$ vs. $V_\perp$, where $V_\parallel = v_z$ and $V_\perp = \sqrt{v_x^2 + v_y^2}$. Each 2D bin then consisted of the average PSD corresponding to a given pair of velocities, $(V_\perp V_\parallel)$. These 2D distributions were computed at the 10 sec cadence of the 3D VDFs and then averaged over the selected upstream and downstream intervals. This results in our final upstream and downstream 2D distribution. In order to identify how He^+ PUI distributions change across the shock and relative to the magnetic field, we integrated each 2D distribution over the parallel and perpendicular direction. This resulted in 1D distributions ($f(V_\parallel)$ and $f(V_\perp)$) defined by

$$f(V_\parallel) = \sum_{V_\perp} 2\pi\, f(V_\parallel, V_\perp)\, V_\perp\, \Delta V_\perp, \tag{3}$$

$$f(V_\perp) = \sum_{V_\parallel} 2\pi\, f(V_\parallel, V_\perp)\, V_\perp\, \Delta V_\parallel, \tag{4}$$

Each phase space contribution to an integral is the average phase space within the contributing phase space pixel.

In order to identify signs of energization in the perpendicular direction, we also computed 1D perpendicular PSD slices by averaging the 2D distributions in the parallel dimension near $V_\parallel = 0\, km\, s^{-1}$. These PSD slices are defined by

$$f_{slice}(V_\perp) = \sum_{|V_\parallel| \le 60\frac{km}{s}} f(V_\parallel, V_\perp). \tag{5}$$

These slices were computed for both upstream and downstream distributions.

3.2 Solar Wind Contamination

When the HPCA instrument measures environments with high proton fluxes, such as the solar wind and magnetosheath, uncorrelated coincidence counts are recorded in the TOF section of the instrument. These counts are recorded in all TOF bins including those for He^+ and are highest solar wind energies.

These so called "bleed-over" counts have been discussed by Gomez *et al.* (2019), Starkey *et al.* (2019), and Starkey *et al.*, (2020), and must be removed in order to isolate the true He^+ signal. To minimize bleed-over counts, energy channels corresponding to solar wind proton energies are removed from all He^+ distributions. Thus, we only analyze the higher energy portion of the PUI distribution. In HPCA survey mode, due to telemetry constraints, counts from every four energy steps are summed together. Since all of the data shown in this paper was acquired in survey mode, we consecutively removed blocks of 4 energy channels from the distributions in order to remove the bleed-over signal. To determine the appropriate energy channels to remove, we first plotted reduced 2D distributions in the spacecraft frame and in GSE coordinates. These 2D distributions are formed by simply summing over the z_{gse} dimension. Figure 2 is an example of such a distribution for the upstream interval of the bow shock event S4. In both panels, the origin represents the spacecraft frame and the black box is the projected bulk plasma frame. The black arrow is the projection of the magnetic field vector, averaged over the time interval shown at the top of both panels. The left panel shows the He^+ distribution without removing any energy channels, while the right panel shows the same distribution, but with counts from energy channels 0-43 (1.35 – 1639.35 eV) removed (note the change in the color bar scale in the right panel). In the left panel, the bleed-over proton signal is the PSD (yellow spot) located at $(V_x, V_y) \cong (-150, 0)\ km/s$. The bleed-over counts are recorded in He^+ TOF bins corresponding to solar wind proton energies. Since these counts are registered as He^+ ions, when converted to He^+ velocity they appear with speeds lower than the bulk proton speed by the factor $\sqrt{\frac{m_{He}}{m_H}} = 2$. In the right panel, the majority of the bleed-over proton signal has been removed and we are left with the high-energy portion of the He^+ PUI distribution. We performed the same analysis for all shocks in order to remove the bleed-over proton signal. In all cases, we removed energy channels 0-43 (1.35 – 1639.35 eV) or 0-47 (1.35 – 3173.78 eV) depending on the solar wind energy.

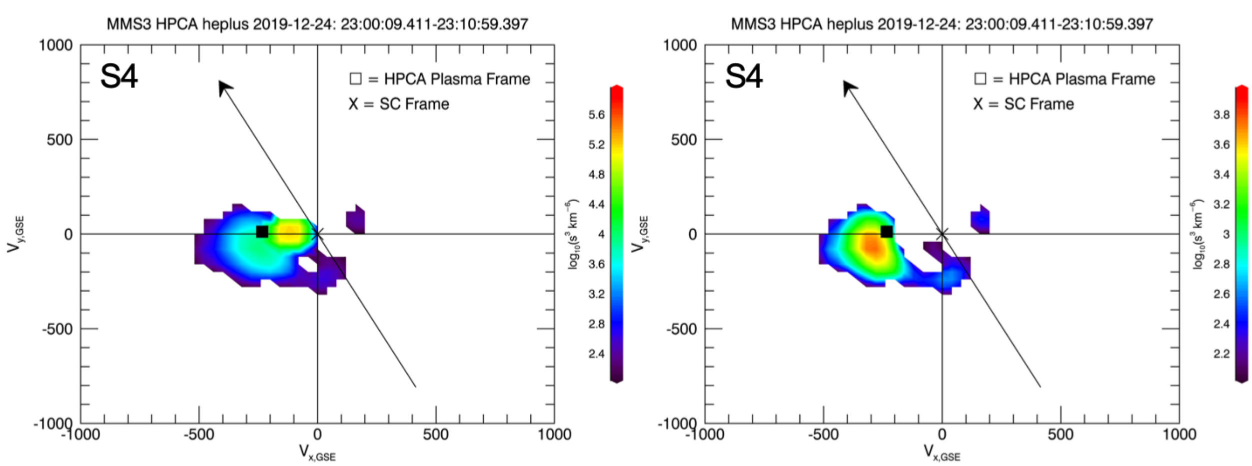

Figure 2. Comparison plot of 2D He^+ PSD distributions in the GSE x-y plane. The distributions were measured by MMS3 and summed over the z_{GSE} dimension. The black arrow in both plots is the projection of the upstream magnetic field direction. The origin represents the spacecraft frame, while the black box represents the projection of the upstream bulk solar wind velocity vector. The left plot shows the distribution with all HPCA energy channels included while in the right plot, energy channels 0-43 (1.35 – 1639.35 eV) have been removed.

4. Results

We compared upstream and downstream distributions in order to identify signs of preferential heating/energization relative to the local magnetic field. We first discuss the form of the upstream PUI distributions that we observed. We next compare $f(V_\parallel)$, upstream and downstream of each shock, and quantify the observed parallel heating. Then, we compare $f(V_\perp)$ across the shock and discuss the observed signs of heating and preferential ion energization in the perpendicular direction. Lastly, we compare the change in power-law indices of $f_{slice}(V_\perp)$ across the shock to M_f.

4.1 Upstream PUI Distributions

We compared 2D He^+ VDFs from the upstream regions of each shock in order to determine and categorize their form. Theoretically, initial PUI distributions are expected to form a ring-like distribution in the bulk plasma frame, whose outward normal to the plane of the ring aligns with the local magnetic field direction and with radius $V_{sw}\sin(\alpha)$, where α is the angle between the magnetic field and bulk solar wind velocity. When $\alpha < 90°$, the PUI distribution's guiding center motion will have a component parallel to the field. Thus, these distributions are referred to as ring-beam distributions. For the purposes of this paper, we will refer to them as ring distributions. This ring can then evolve into a shell-like distribution due to pitch-angle scattering. In our 2D distributions, an ideal PUI ring distribution would appear as a localized spot of high PSD located near $V_\parallel = 0$ km/s (depending on α) and $V_\perp = V_{sw}$, whereas an ideal shell distribution should have PSD distributed around the arc defined by $\sqrt{V_\perp^2 + V_\parallel^2} = V_{sw}$. Note that since our 2D distributions are gyrophase-averaged, we are unable to distinguish between a gyrotropic and gyrophase-bunched distribution.

Figure 3 shows a comparison between measured and theoretically modelled ring distributions and shell distributions in the plasma rest frame. Panels a) and b) show measured upstream 2D VDFs from events S10 and S2, respectively, while panels c) and d) show 2D modelled distributions of an ideal shell and ring distribution, respectively. Panel a) is representative of a shell-like distribution due to the high PSD located within the arc $v = {\sim}400$ km/s. Furthermore, the radius of the measured shell distribution agrees well with the measured upstream solar wind speed ($V_{sw} = 392$ km/s) (Starkey et al., 2019). On the other hand, panel b) is representative of a ring distribution due to the high PSD contributions centered near $V_\parallel = 50$ km/s and within $V_\perp = 300$ km/s, which agrees well with the measured solar wind speed for this event of $V_{sw} = 298$ km/s. Due to the Gaussian falloff of the model ring distribution, centered on V_{sw}, the model ring distribution has significant PSD contributions beyond $V = V_{sw}$ as opposed to the sharp cutoff that is observed in the data. Note that the offset from $V_\parallel = 0$ km/s of the peak phase space density in the right panel is likely due to the underestimation of the HPCA bulk velocity vector, which is used to define our frame transformation. We also note that the underestimation of the HPCA SW velocity vector may result in additional stretching of the upstream 2D distributions in the perpendicular direction. However, we still observe a sharp drop in PSD in the upstream 2D distributions for $V > V_{sw,HPCA}$, which is consistent with expected PUI SW distributions. Thus, the underestimation of the HPCA SW vector should not significantly affect the results of this paper. We see that the measured shell and ring VDFs compare well to their modelled counterparts, respectively. Note that since we removed lower energy channels from our VDFs (due to bleed-over proton counts), we do not see PSD contributions near $V_\parallel = 0$ km/s.

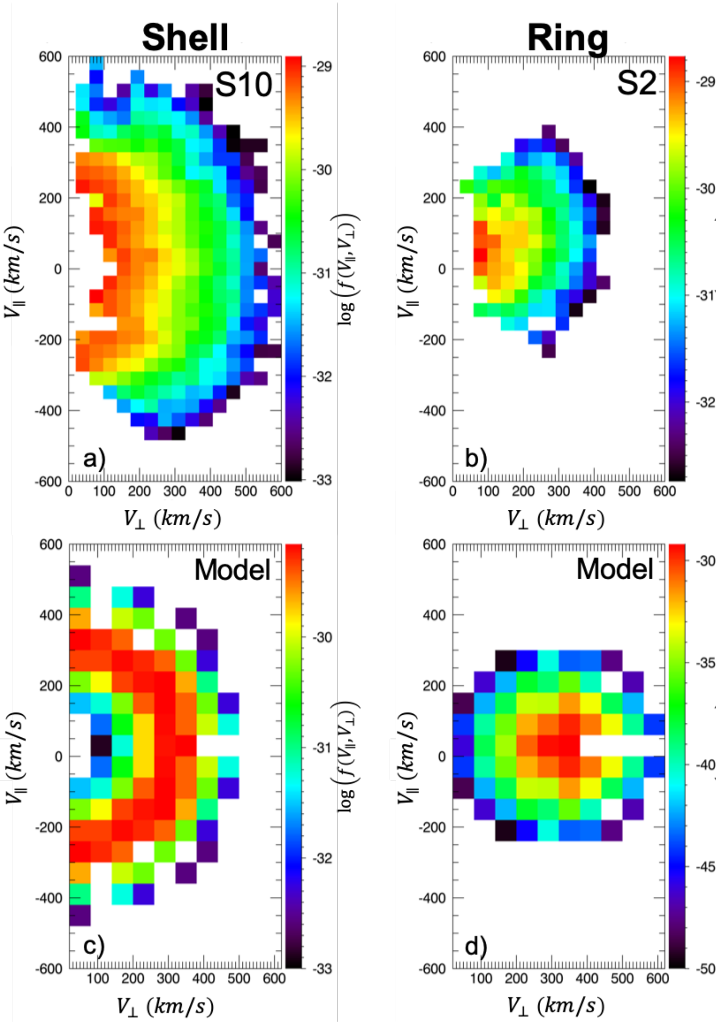

Figure 3. Examples of upstream 2D He^{+} VDFs computed from Eq. 2. Panel a) shows event S10 and panel b) shows event S2. Panels c) and d) show modelled shell and ring distributions, respectively. Each plot shows the gyrophase averaged PSD with the parallel velocity on the y-axis and perpendicular velocity on the x-axis, relative to the magnetic field. The left plots correspond to PUI shell distributions and the right plots correspond to PUI ring distributions.

To classify the form of the upstream VDFs from the 10 events studied in this paper, we defined 4 categories: shell, partial shell, ring, undetermined. The results of this classification are shown in Fig. 4 and are as follows: 4 shell, 3 partial-shell, 2 ring, and 1 undetermined. The distributions thus tend to resemble shell or partial shell distributions for the majority of the cases. Note that the single undefined distribution (corresponding to S4) contained a high energy population of He^{+} ions centered on $(V_\perp = \sim 2V_{sw}, V_\parallel = 0)$ in the 2D distribution. This population was in addition to what we would have considered a ring-like distribution.

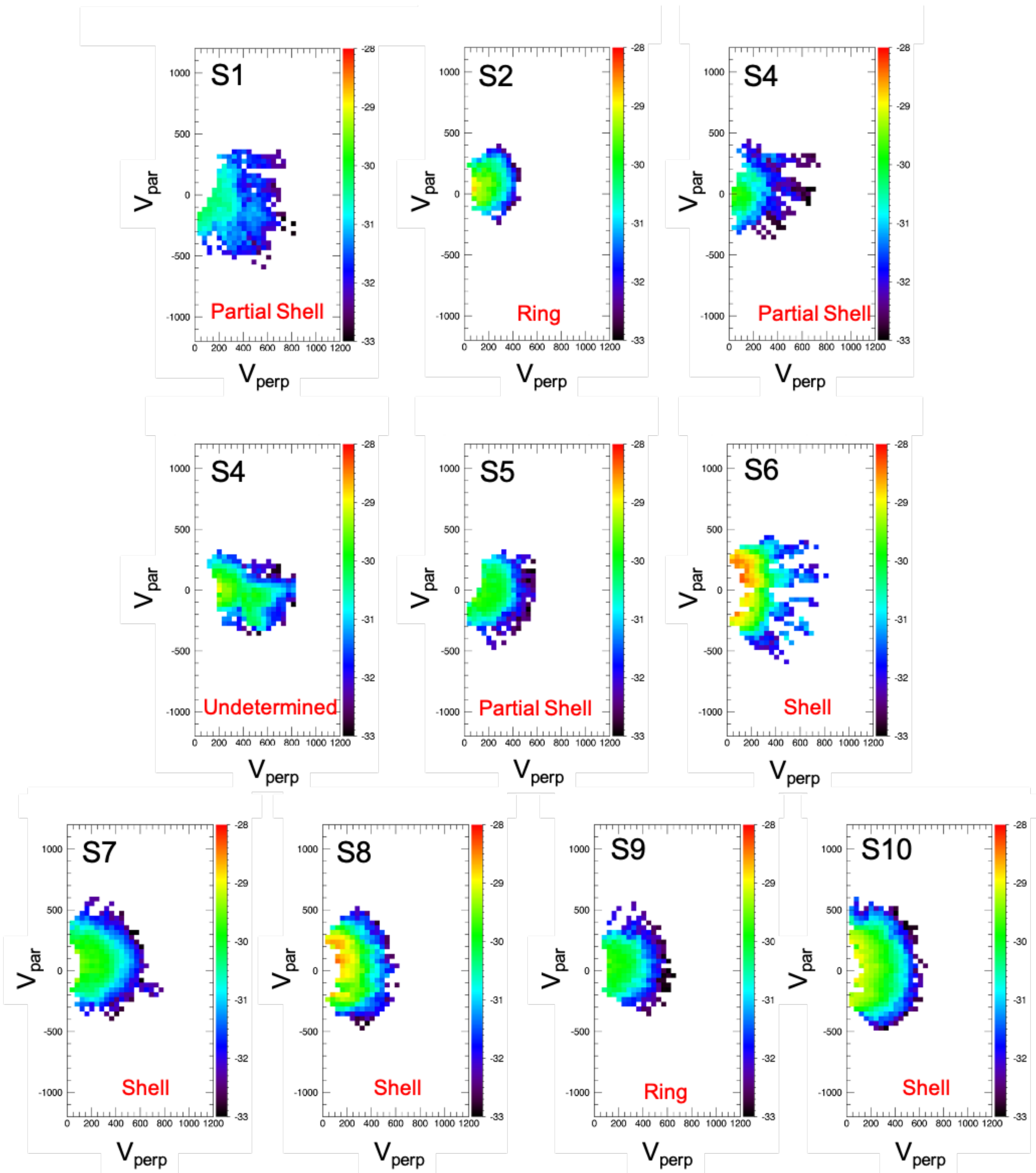

Figure 4. Upstream 2D He+ VDFs for each of the 10 shocks. The event label is shown in the top left corner of each plot and the classification for each distribution is shown in red at the bottom of each plot.

4.2 Comparison of Parallel Distributions

In this subsection we discuss our results obtained from comparing upstream to downstream $f(V_{\|})$. In order to quantify the relative amount of heating that occurred across each shock, we estimated the temperature of the upstream and downstream $f(V_{\|})$ using 1D Maxwellian fits of the distributions. Figure 5 shows the resulting upstream to downstream comparisons for each shock event. The panels are ordered by increasing M_f (S1–S10) from left to right and downward. Each panel of the figure corresponds to a different shock (labelled in the top left corner) and shows $f(V_\parallel)$ upstream (red) and downstream (blue) of the shock. The classification of the upstream 2D distribution is shown in the top left corner of each panel, below the event label. The magenta lines are the Maxwellian fits for both distributions. The temperatures of the Maxwellian fits are then shown in the top right corner, and are color coded to the upstream and downstream intervals. The ratio of these temperatures is also shown in magenta.

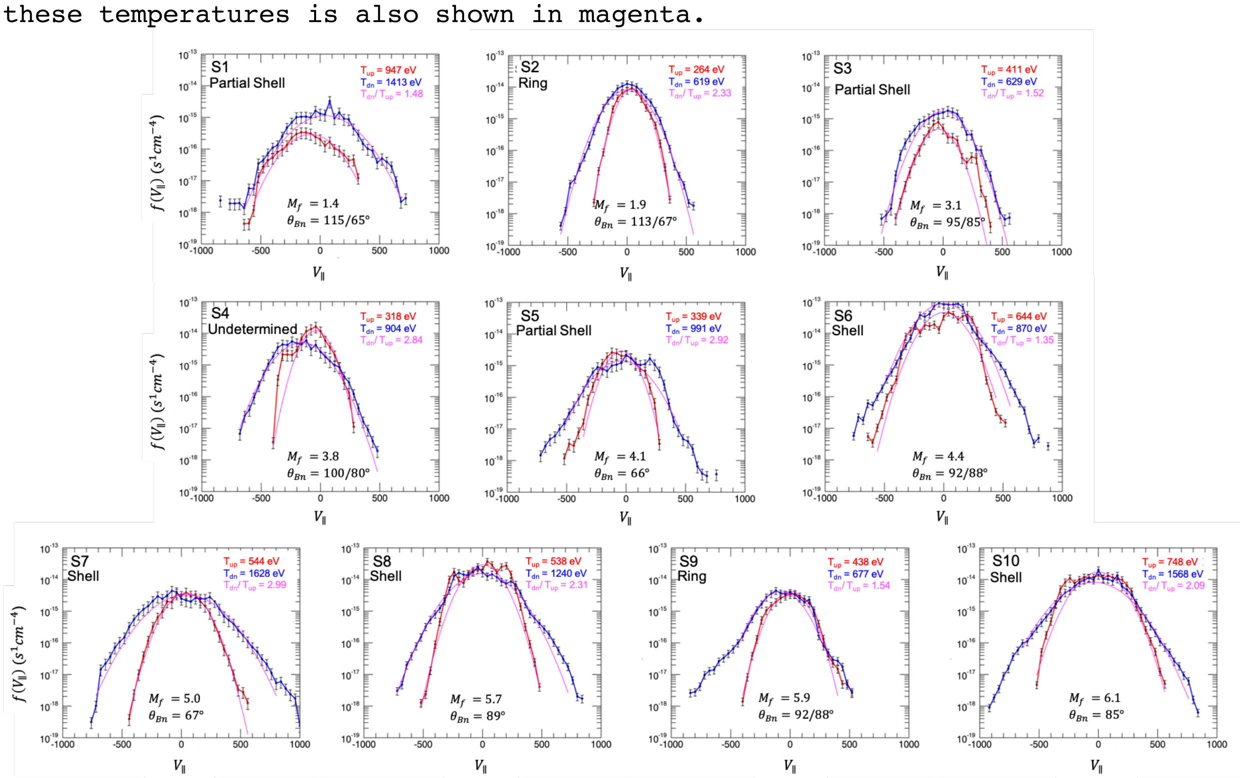

Figure 5. Comparisons of $f(V_\parallel)$, upstream (red) and downstream (blue) of each shock event (labelled in the top right corner of each panel). The classification of the upstream 2D distribution is shown in the top left corner of each panel, below the event label. The magenta curves are the Maxwellian fits to each distribution and the resulting temperature values are shown in the top right corner of each panel, color coded to the upstream/downstream interval. The ratio of the resulting temperatures is also shown in the top right corner of each panel.

From Fig. 5, we see that in all cases $f(V_\parallel)$ have been heated across the shock. However, if we first restrict our attention to shocks with $\theta_{Bn} \le 70°$ (S1, S2, S5, and S7), it appears that the core of the downstream parallel distribution has broadened relative to the core of the upstream distribution. On the other hand, for shocks with $\theta_{Bn} \ge 80°$ (S3, S4, S6, S8, S9, and S10), the core of the downstream distribution seems to track the core of the upstream distribution closely with less broadening than the shocks with $\theta_{Bn} \le 70°$. However, the tails of these distributions extend to higher speeds and exhibit a distinct change in the slope of the distribution away from the Maxwellian core. This feature is more pronounced for higher Mach shocks and is not generally seen in the downstream distributions of shocks with $\theta_{Bn} \le 70°$. These results thus suggest that for lower θ_{Bn} and M_f, the evolution of the distribution across the shock is dominated by core heating. On the other hand, for higher θ_{Bn} and M_f, the downstream distributions show signs of a combination of heating and energization due to the broadening of the cores and the divergence of the tails from a pure Maxwellian distribution, respectively.

It has been shown by Pesses (1981b) that the first adiabatic invariant (μ_B) is on average conserved at perpendicular shocks. We would then expect the heating across the shock to scale with magnetic compression ratio. Thus, the ratio of temperatures across the shock should be equal to the magnetic compression ratio if the heating was due to solely to the conservation of μ_B. Note that the conservation of μ_B initially leads to perpendicular heating, but with sufficient scattering this heat can be redistributed into the parallel direction. In order to quantify the relative amount of heating that occurs across each shock and to investigate this relation, we plotted the ratio, $(T_{\parallel,dn}/T_{\parallel,up})/(B_{dn}/B_{up})$, against M_f in Fig. 6. Here, $T_{\parallel,dn}$ and $T_{\parallel,up}$ are the downstream and upstream temperatures derived from the Maxwellian fits of $f(V_\parallel)$, respectively. The quantity B_{dn}/B_{up} is the transverse magnetic compression ratio from Table 1. The data points are color coded to θ_{Bn}, and the error bars correspond to the 1-σ uncertainties in the computed temperature values. Note that since the perpendicular distributions are non-Maxwellian in nature, we can only estimate their temperatures by performing a second order moment calculation. However, due to the removal of lower energy channels, these calculations are not accurate and are not an appropriate comparison to the Maxwellian-derived parallel temperatures. Thus, we do not provide perpendicular temperature calculations in this paper. If we focus on the blue points first, for which $\theta_{Bn} \leq 70°$, we see that the ratio is near 1 for the shocks with $M_f > 1.5$. A ratio of 1 suggests that the observed heating may be due to the conservation of μ_B, where we have assumed that there is sufficient scattering to redistribute the heat from the perpendicular to the parallel direction. On the other hand, for shocks with $\theta_{Bn} \geq 80°$ (red points), the ratio is less than 1 and decreases slightly with increasing M_f. This suggests that either other mechanisms contribute to the parallel heating, or that there is insufficient scattering to redistribute the perpendicular heating resulting from the conservation of μ_B. Of course, this may also be due to a combination of the two. Since the downstream distributions are not isotropic, but highly anisotropic, we do not attempt to estimate the amount of energy transferred to the parallel component. These results suggest that the significance of heating via adiabatic compression may depend on θ_{Bn}, and is likely stronger for lower θ_{Bn}, but that other non-adiabatic processes (e.g., SDA) are required to account for the observed level of heating across the shock as M_f increases.

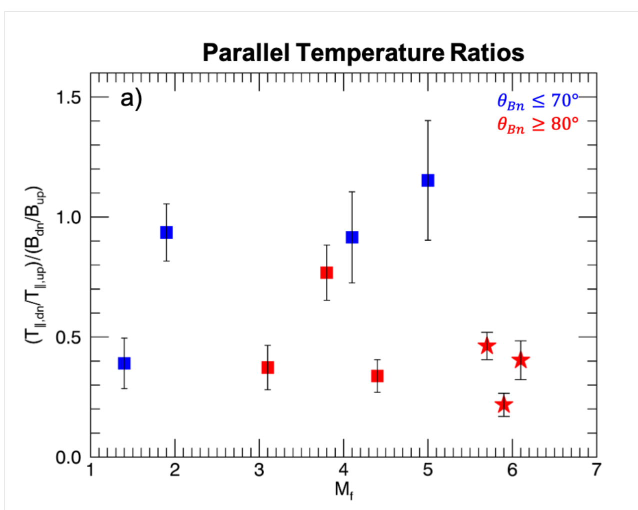

Figure 6. Plot showing the downstream-to-upstream ratio of parallel temperatures divided by the magnetic compression ratio as a function of M_f, for each shock. The data points are color coded to θ_{Bn} and the error bars are calculated using the 1-σ uncertainties of the temperature values. The starred data points indicate events S8, S9, and S10 for which the magnetic compression ratio was > 4.

4.3 Comparison of Perpendicular Distributions

We next compared $f(V_\perp)$ across the shock in order to identify signs of perpendicular energization of the He^+ PUIs. Similar to Fig. 5, we compare $f(V_\perp)$ upstream and downstream of each shock in Figure 7. The panels are ordered by increasing M_f from left to right and downward, with the event label shown in the top right corner. Each panel shows the upstream (red) and downstream (blue) $f(V_\perp)$ plotted against perpendicular speed normalized by the SW speed, $V_\perp/V_{sw}$. In all cases (except S4), the downstream distribution extends to higher speeds and the slope has flattened. For the shocks with $\theta_{Bn} \leq 70°$ (S1, S2, S5, and S7), the downstream distribution is broader with tails extending to higher speeds. Similar to observations made from Fig. 5, this suggests that the core of these distributions is heated across the shock, however the tails are more suggestive of energization. On the other hand, for shocks with high M_f and $\theta_{Bn} \geq 80°$ (S6, S8, S9, and S10), the core of the distribution has broadened and the downstream distributions exhibit a distinct change in slope that extends to much higher velocities. This effect is much more pronounced for the higher Mach shocks, and is not quite evident in events S3 and S4 (whose downstream distributions tend to resemble the upstream distributions). This distinct change in the shape of the distribution differentiates these spectra from those in Figure 5 and indicates that ions are being energized perpendicular to the field, and that the level of this energization is stronger for shocks with higher θ_{Bn} and M_f.

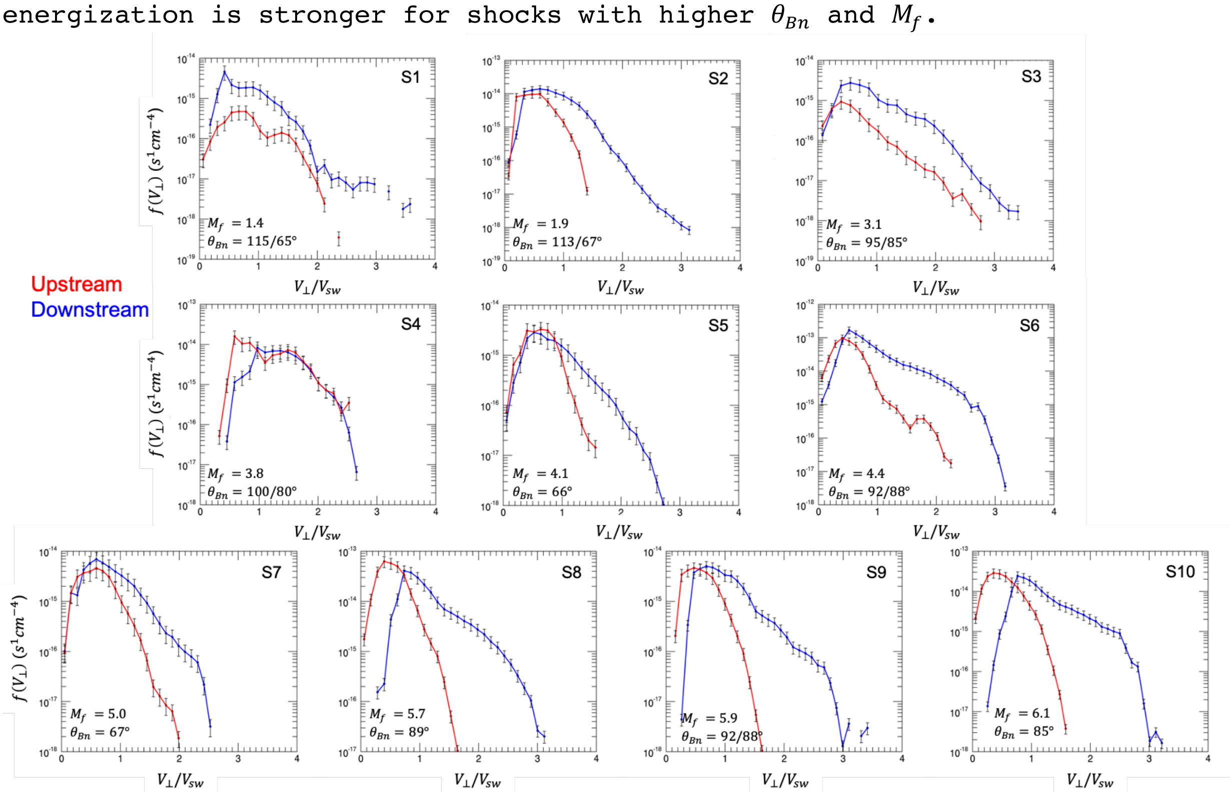

Figure 7. Comparisons of $f(V_\perp)$, upstream (red) and downstream (blue) of each shock event (labelled in the top right corner of each panel). The x-axis has been normalized to the measured solar wind velocity corresponding to each event.

In order to quantify the observations of perpendicularly energized He^+ ions from Fig. 7, we next computed $f_{slice}(V_\perp)$ upstream and downstream of each shock. The high energy tails of each of these distributions were then fit to a power-law in velocity: $f_{slice}(V_\perp) \propto V_\perp^{-\eta}$. This resulted in a spectral index for both the upstream and downstream distribution (η_{up} and η_{dn}). The velocity range of the fit depended on where the distributions exhibited a power-law for speeds $\geq \sim V_{sw}$. The resulting upstream and downstream $f_{slice}(V_\perp)$ distributions and their power-law fits are shown in Fig. 8. The format of this figure is the same as Fig. 5 and Fig. 7, and the event label is shown in the top left corner of each plot. Each panel shows the upstream (red) and downstream (blue) $f_{slice}(V_\perp)$, plotted agains normalized speed $V_\perp/V_{sw}$. The magenta lines are the power-law fits to each distribution and the resulting indices are shown in the top right corner, color-coded to the upstream and downstream intervals. The upstream-to-downstream power-law ratio is also shown in magenta in the top right corner. For higher M_f (S5-S10), the downstream distribution ehxibits a clear power-law that has become shallower than that of the upstream distribution. Furthermore, at the lower M_f shocks (S1-S3) there does not seem to be any significant flattening of the downstream distribution.

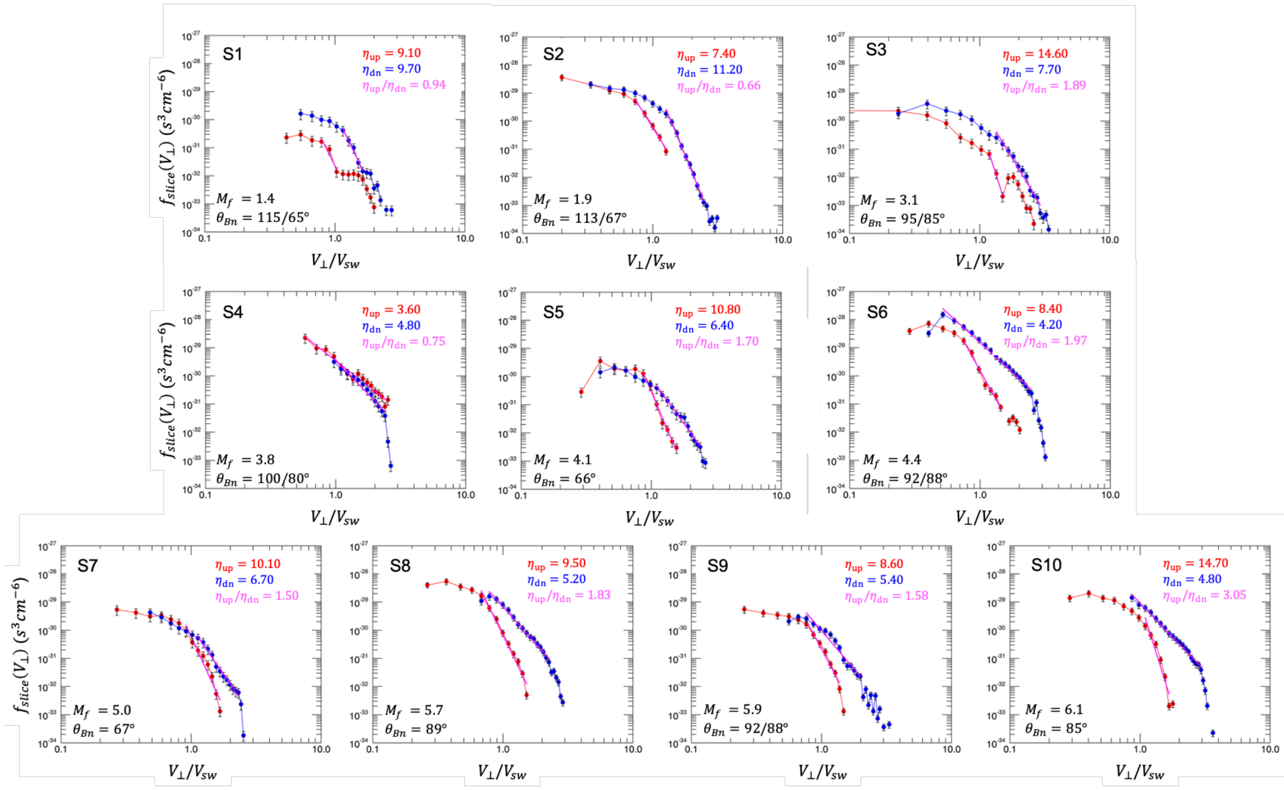

Figure 8. Comparisons of $f_{slice}(V_\perp)$, upstream (red) and downstream (blue) of each shock event (labelled in the top left corner of each panel). The x-axis has been normalized to the measured solar wind velocity corresponding to each event. The magenta lines are the power-law fits to the tails of each distribution, and the resulting power-law indices (η_{up} and η_{dn}) are shown in the top right corner of each panel. The upstream-to-downstream ratio of power-law indicies is also shown in the top right corner of each panel.

Lastly, Figure 9 shows the power-law ratio, η_{up}/η_{dn}, versus M_f. The error bars are determined from the 1-σ uncertainties of the spectral indices obtained from the power-law fits. A ratio larger than 1 means that the perpendicular distribution has flattened across the shock, and is indicative of energization/heating in the perpendicular direction. From the figure, it appears that for lower Mach shocks this ratio is close to ~1, while for higher Mach shocks the ratio tends towards ~2 (excluding the outlier with a ratio of ~3). Thus, for higher Mach shocks the downstream distribution is perpendicularly energized, resulting in a high-energy power-law tail. The formation of such a power-law tail provides support for ion energization by drift mechanisms such as SDA. Furthermore, due to the underestimation of the HPCA SW velocity, additional stretching of the upstream 2D distribution may occur in the perpendicular direction. This may result in the overestimation of the upstream perpendicular heating, which would decrease the magnitude of η_{up} as well as the ratio η_{up}/η_{dn}. Therefore, the power-law ratio is likely a lower bound on the observed heating/energization. These results confirm that He^+ PUIs are preferentially energized perpendicular to the local magnetic field, and that this energization becomes stronger with increasing M_f.

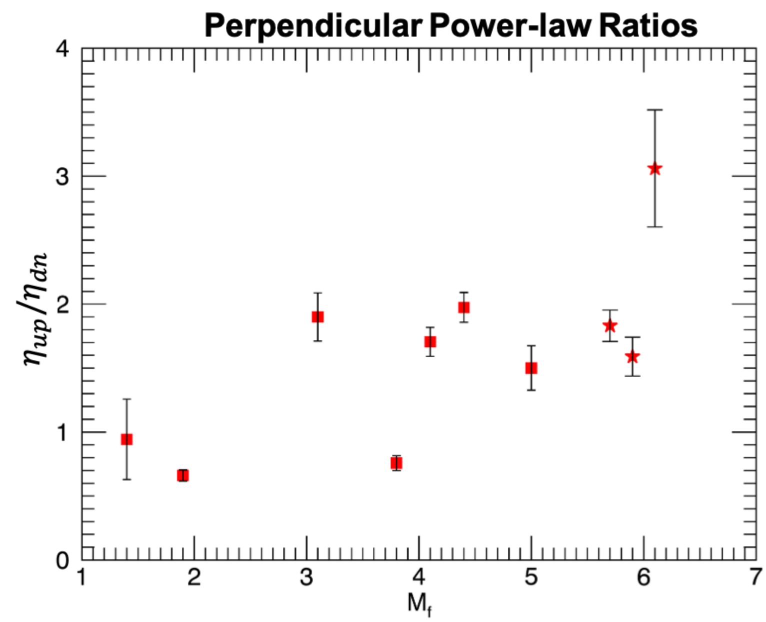

Figure 9. The ratio of upstream to downstream power-law index derived from $f_{slice}(V_\perp)$, for each shock versus M_f. Error bars are calculated using the 1-σ uncertainties of the power-law indices obtained from the power-law fit. The starred data points indicate events S8, S9, and S10 for which the magnetic compression ratio was > 4.

5. Discussion

For each of the 10 events analyzed in this paper, we first analyzed 2D He^+ VDFs upstream of the shock and characterized the distributional form. We found that the majority of cases resembled shell or partial shell distributions. Note that the formation and evolution of He^+ ring-beam distributions, while outside the scope of this paper, has been extensively studied using data from the STEREO spacecraft (Drews et al., 2013, 2015) and data from the GEOTAIL spacecraft (Oka et al., 2002a). These works helped to reveal underlying complexities regarding the He^+ PUI ring distribution. Thus, the observations presented in this work help to inform the study of PUIs in the solar wind at 1 AU.

We next analyzed $f(V_\parallel)$ in terms of heating across the shock. For all events, the cores of the distribtuions broadened across the shock, indicating parallel heating. However, for higher θ_{Bn} and M_f, the tails of the downstream distributions diverged from the Maxwellian core indicating a combination of heating and energization. Based on work by Pesses (1981b), we expect that the heating across the shock should scale with the magnetic compression ratio. Assuming sufficient scattering in the downstream, this scaling would then apply to the ratio of parallel temperatures across the shock. In order to investigate the parallel heating observed in this paper, we compared the ratio of parallel temperatures normalized by the magnetic compression ratio to M_f (Fig. 6). We found a dependance on θ_{Bn} such that shocks with $\theta_{Bn} \leq 70°$ had ratios ~1 (aside from the shock with the lowest M_f), while shocks with $\theta_{Bn} \geq 80°$ had ratios <1 which decreased with increasing M_f. Typically, for lower θ_{Bn} it is easier for ions to stream back and forth across the shock, thus scattering in the downstream region is more likely and heat is more easily redistributed from the perpendicular to the parallel direction. It appears then that adiabatic compression likely contributes to the parallel heating for quasi-perpendicular shocks (for which scattering in the downstream region is more likely), but that the level of contribution is smaller for nearly perpendicular shocks as other processes become dominant (e.g., SDA).

We next investigated the change in $f(V_\perp)$ across the shock and observed signs of preferential energization in the perpendicular direction. Downstream of the high Mach and nearly perpendicular shocks, the tail of $f(V_\perp)$ exhibited a distinct change in slope away from the core of the distribution and rather different than those observed for parallel distributions. This tail then extended to high speeds, indicating that the ions had been strongly energized in the perpendicular direction. In order to quantify this preferential energization, we compared the ratio of upstream-to-downstream power-law indices with M_f. We observed a clear increasing trend in η_{up}/η_{dn} with M_f, indicating that the relative amount of energization was larger for higher Mach shocks. These results are consistent with the theory of DSA in the form of drift acceleration mechanisms such as SDA. As shown in Jokipi (1982), as the shock angle tends towards 90°, the energy gain becomes entirely due to particle drifts through the $\vec{V} \times \vec{B}$ electric field. This tendancy then results in strong energization in the perpendicular direction. Furthermore, as the Mach number increases, so does the magnitude of $\vec{V}_{sw}$ normal to the shock, which in turn increases the magnitude of the upstream $\vec{V} \times \vec{B}$ electric field in the shock frame. Thus, the amount of energization in the perpendicular direction should increase with increasing Mach number. Based on Jokipi (1982), this effect should then be more pronounced for shocks with θ_{Bn} closer to 90°. In the theory of pure SDA at perpendicular shocks, the energy gain is due to magnetic gradient drift and is proportional to the magnetic compression ratio. This implies that the final energy of an ion, energized via SDA, is proportional to the ion's initial energy and that the spectral shape of the distribution does not change across the shock. Our results from Fig. 9 show that at low M_f, the power-law ratio tends towards ~1, while at higher M_f the ratio tends towards ~2. Thus, we suggest that at low M_f, pure SDA is responsible for the observed perpendicular energization, leading to no spectral change across the shock and hence a power-law ratio of $\eta_{up}/\eta_{dn} = \sim 1$. On the other hand, for higher M_f, other energization mechanisms such as SR, SS, and MRI contribute towards the flattening of the spectrum across the shock.

In DSA theory, it is well established that the power-law spectrum of shock accelerated ions depends only on the compression ratio of the shock (Jones & Ellison, 1991). The downstream solution to the diffusion-convection equation in the local plasma frame exhibits a power-law tail, whose index (σ) is related to the compression ratio by $\sigma = \frac{3r}{r-1}$. In order to compare our results with these theoretical expectations we plotted this relation using our estimates of the magnetic compression ratio ($r = \frac{B_{dn}}{B_{up}}$; see Table 1) and the downstream spectral indices derived from $f_{slice}(V_\perp)$. Note that typically the compression ratio from the transverse magnetic field also depends on other parameters such as θ_{Bn}, v_A, and the normal flow speed. However, for the events presented here (quasi-perpendicular and high Mach shocks) this dependance is negligible and $r = \frac{B_{dn}}{B_{up}}$ is a valid assumption. The results are shown in Fig. 10 which plots η_{dn} against $\frac{3r}{r-1}$. The data points are color coded to the shock angle and the error bars are the 1-sigma uncertainties of the estimated spectral indices. Interestingly, the data points for shocks with $\theta_{Bn} \geq 80°$ are closer to the theoretical prediction (dashed line) than those with $\theta_{Bn} \leq 70°$. We note however that this theoretical relation relies on the assumption of isotropy and an ideal plasma. However, PUIs are not required to behave as such an isotropic ideal gas. Thus, the discrepancy between theory and observations shown in Fig. 10 is likely due to the underlying assumptions of the theory.

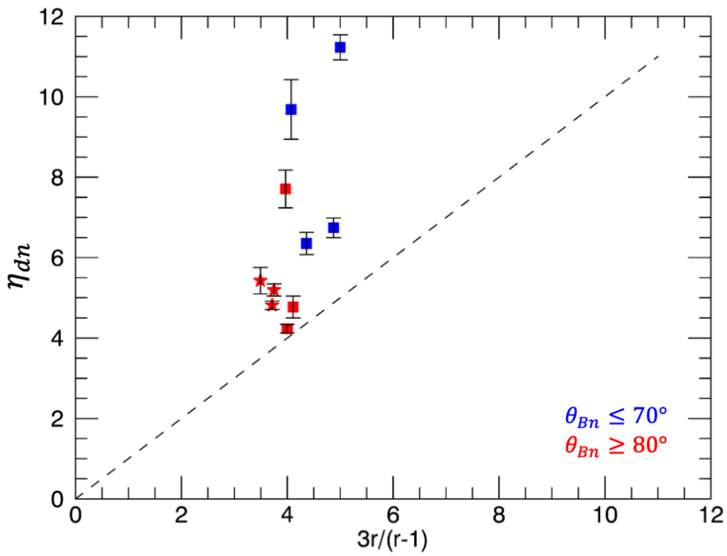

Figure 10. Plot showing the theoretically predicted versus measured power-law index of the downstream distributions. The measured index, η_{dn}, is calculated from $f(V_{\perp})$ and the value r, is the magnetic compression ratio. The dashed line is the theoretical prediction of DSA. The starred data points indicate events S8, S9, and S10 for which the magnetic compression ratio was > 4.

Lastly, these observations of preferentially energized He^{+} PUIs, perpendicular to the magnetic field, have strong implications for the ion dynamics of the termination shock. At the termination shock, H^{+} PUIs dominate the solar wind pressure and are thus thought to be heavily involved in the shock formation and mediation process (Holzer, 1972; Lee & Axford, 1988; Donohue & Zank, 1993). While the conditions at the termination shock are different from those at the Earth's bow shock, which is mediated by solar wind protons, the termination shock is still thought to be an efficient accelerator of PUIs, which then forms the seed population for ACRs. ACRs are thought to form when PUIs in the solar wind are accelerated at the quasi-perpendicular termination shock along the shock (Pesses et al., 1981a). The accelerated PUIs then charge exchange and become neutral particles. Depending on their velocity at the moment of charge exchange, these high-energy fresh neutrals can travel towards the inner heliosphere and be observed as energetic neutral atoms (ENAs). Our results show that quasi-perpendicular shocks are efficient at accelerating He^{+} PUIs perpendicular to the local magnetic field. Furthermore, for stronger shocks (higher Mach) the acceleration is enhanced. Our observations are consistent with results from Zirnstein et al., (2018) in which preferential heating of H+ PUIs across an interplanetary shock was reported. They found that the H^{+} PUIs contained almost half of the downstream energy flux in the shock frame. The results of our paper, combined with those of Zirnstein et al., 2018, show that PUIs can be efficiently energized at quasi-perpendicular shocks. The shock analyzed in Zirnstein et al., 2018 was observed at ~34 AU, thus providing evidence that PUIs are capable of being accelerated at shocks for which PUIs play a non-trivial role in the shock mediation. Putting it all together, these combined results support the theory of ACR formation and can be used to further understand the physics surrounding the termination shock.

6. Conclusions

In this paper, we analyzed He^{+} PUI distributions upstream and downstream of 10 quasi-perpendicular shocks observed by MMS. These shock observations covered the parameter space of quasi-perpendicular and high-Mach shocks, defined by $\theta_{Bn} \in [60°, 90°]$ and $M_f \in [1,7]$. We characterized the upstream PUI distributions, finding that a majority of the distributions resembled shell or partial shell distributions in the bulk plasma frame. We next compared 1D VDFs across the shock and relative to the local magnetic field. We observed signs of parallel heating and quantified this by fitting Maxwellian functions to the core of the $f(V_\parallel)$ distributions. We then compared the ratio of parallel temperatures, normalized by the magnetic compression ratio, to M_f. The ratio was near 1 for quasi-perpendicular shocks and less than 1 and decreasing for nearly perpendicular shocks. This suggests that parallel heating resulting from the conservation of μ_B depends on the shock geometry and the level of scattering occurring downstream of the shock. Next, we compared upstream and downstream $f(V_\perp)$ distributions which revealed signs of energization in the perpendicular direction, particularly in the tail of the spectra. To quantify this energization and relate it to M_f, we calculated the ratio of upstream to downstream power-law indices from the tails of the $f_{slice}(V_\perp)$ distributions. This ratio was observed to increase with increasing M_f, indicating that ions are preferentially energized in the perpendicular direction more efficiently at higher Mach shocks.

7. Acknowledgments

This work was funded by NASA grant 80NSSC18K1366 and by MMS contract number NNG04EB99C. The MMS data sets used are accessible through the MMS Science Data Center website located at (https://lasp.colorado.edu/mms/sdc/public/). Wind data were obtained from the GSFC/SPDF OMNIWeb website (http://omniweb.gsfc.nasa.gov).

References

Baring, M. G. 1997, arXiv:astro-ph/9711177v1

Burgess, D., Möbius, E., & Scholer, M. (2012), Ion acceleration at the Earth's bow shock, *Space Sci. Rev.*, 173:5-47, doi:1 0.1007/s11214-012-9901-5.

Caprioli, D., Amato, E., & Blasi, P. (2010), Non-linear diffusive shock acceleration with free- escape boundary, J. *Astroparticle Phys.*, 33, 5-6, 307-311, doi: 10.1016/j.astropartphys.2010.03.001

Caprioli, D., Pop, A-R., & Spitkovsky, A. (2015), Simulations and theory of ion injection at non-relativistic collisionless shocks, *Ap. J. Lett.*, 798, L28, doi:10.1088/2041-8205/798/2/L28

Chen, G., and T. P. Armstrong, 1975, *Proc. Int. 14th Cosmic Ray Conf.*, 5,1814.

Cohen, I. J., Schwartz, S. J., Goodrich, et al. 2019, *J. Geophys. Res.: Space Physics*, 124, 3961–3978. https://doi.org/ 10.1029/2018JA026197

Decker, R. B., 1981, *J. Geophys. Res.*, 86, 4537.

Decker, R. B., 1983, *J. Geophys. Res.*, 88, 9959.

Decker, R. B., & L. Vlahos, 1986, *J. Geophys. Res.*, 91, 13,349.

Desai, M. I., G. M. Mason, J. R. Dwyer, J. E. Mazur, T. T. von Rosenvinge, and R. P. Lepping (2000), Characteristics of energetic (>30keV/nucleon) ions observed by the Wind/STEP instrument upstream of the Earth's bow shock, J. Geophys. Res., 105, 6178, doi:10.1029/1999JA900406.

Desai, M. I., Mason, G. M., Wiedenbeck, M. E., et al., 2004, *Astrophys. J.*, **611**(2), 1156–1174, doi:10.1086/422211.

Desai, M. I. & Burgess, D. (2008), Particle acceleration at coronal mass ejection-driven interplanetary shocks and the Earth's bow shock, *J. Geophys. Res.*, 113, A00B06, doi: 10.1029/2008JA013219.

Donohue, D. J. and G. P. Zank, The steady state and dynamical structure of a cosmic-ray- modified termination shock, *J. Geophys. Res.*, 98, 19,005, 1993.

Drews, C., Berger, L., Wimmer-Schweingruber, R. F., & Galvin, A. B. (2013), Interstellar He^+ ring-beam distributions: Observations and Implications. *Journal of Geophys. Res. Lett.*, 40, 1468 -1473. doi:10.1002/grl.50368

Drews, C., Berger, L., Taut, A., Peleikis, T., & Wimmer-Schweingruber, R. F. (2015), 2D He^+ pickup ion velocity distribution functions: STEREO PLASTIC observations. *A&A,* 575(A97). doi: https://doi.org/10.1051/0004-6361/201425271

Ellison, D. C., Jones, F. C., & Baring, M. G. (1999), Direct acceleration of pickup ions at the solar wind termination shock: The production of anomalous cosmic rays, *Astrophys. J.,* 512(1), 403-416.

Fisk, L. A., & Lee, M. A., 1980, *Astrophys. J.,* 237, 620-626.

Fisk, L. A., & Gloeckler, G. (2017), *J. Phys.: Conf. Ser.* **900,** 012006.

Giacalone, J. & Jokipii, J. R. (1995), Simulations of pickup-ion acceleration at quasi-perpendicular shocks. *Space Sci. Rev.*, 72(1/2), 441-446.

Giacalone, J., & Decker, R. (2010), The origin of low-energy anomalous cosmic rays at the solar-wind termination shock, *Ap. J.*, 710, 91.

Gloeckler, G., Geiss, J., Roelof, E. C., Fisk, L. A., Ipavich, F. M., Ogilvie, K. W., Lanzerotti, L, J., von Steiger, R., & Wilken, B. (1994). Acceleration of interstellar pickup ions in the disturbed solar wind observed on Ulysses. *J. Geophys. Res.* 99(A9), 17637-16643.

Gloeckler, G., Geiss, J. (1998), Interstellar and Inner Source Pickup Ions Observed with Swics on Ulysses. *Space Sci. Rev.,* 86(1-4), 127-159.

Gloeckler, G. , Mobius, E., Geiss, J., Bzowski, M., Chalov, S., Fahr, H., McMullin, D. R., Noda, H., Oka, M., Rucinski, D., Skoug, R., Terasawa, T., von Steigger, R., Yamazaki, A., & Zurbuchen, T. (2004a). Observations of the helium focusing cone with pickup ions. *A&A* 426, 845-854. doi:10.1051/0004-6361:20035768

Gloeckler, G., Geiss, J., & Fisk, L. A. (2004b), Heating of pickup and solar wind ions at Jupiter's bow shock, *AIP Conference Proceedings,* **719**, 201 (2004); https://doi.org/10.1063/1.1809518

Gomez, R. G., Fuselier, S. A., Mukherjee, J., Gonzalez, C. A., Burch, J. L., Strangeway, R. J., &   Starkey, M. J. (2019). The extra-magnetospheric ion environment as observed by the Magnetospheric Multiscale mission hot plasma composition analyzer (MMS- HPCA). Journal of Geophysical Research: Space Physics, 124, 1509–1524. https://doi.org/10.1029/2018JA025392

Jokipii, J. R., 1982, *Astrophys. J.,* 255, 716.

Holzer, T. E., Interaction of the solar wind with the neutral component of the interstellar gas, *J. Geophys. Res.*, 77, 5407, 1972.

Jokipii, J. R., 1979, *Proc. 16^{th} int. cosmic ray Conf.,* Kyoto 14, 175.

Jokipii, J. R., 1982, *Astrophys. J.,* 255, 716.

Jones, F. C., & Ellison, D. C. 1991, SSRv, 58, 259

Kota, J., (1979), Drift: The essential Process in Losing Energy, *Proc. 16^{th} Int Cosmic Ray Conf.,* Kyoto 3, 13.

Kucharkek, H., & Scholer, M. (1995), Injection and acceleration of interstellar pickup ions at the heliospheric termination shock, *J. Geophys. Res.,* 100(A2), 1745-1754.

Lee, M. A., 1983, *J. Geophys. Res.*, **88**, 6109–6119, doi:10.1029/JA088iA08p06109.

Lee, M. A., and W. I. Axford, Model structure of a cosmic ray mediated stellar or solar wind, *Astron. Astrophys.*, 194, 297, 1988.

Lee, M. A., Shapiro, V. D., & Sagdeev, R. Z. (1996), Pickup ion energization by shock surfing. *J. Geophys. Res.* 101(A3), 4777-4789.

Leroy, M. M., Goodrich, C. C., Winske, D., Wu, C. S., and Papadopoulos, K. (1981), Simulation of a Perpendicular Bow Shock. *Geophys. Res. Letters,* 8, No. 12, 1269-1272.

Leroy, M. M., Winske, D., Goodrich, C. C., Wu, C. S., Papadopoulos, K. (1982), The Structure of Perpendicular Bow Shocks. *J. Geophys. Res.,* 87, No. A7, 5081-5094.

Mason, G. M., Leske, R. A., Desai, M. I., et al., 2008, *Astrophys. J.*, **678**, 1458–1470, doi:10.1086/533524.

McComas, D. J., Sirnstein, E. J., Bzowski, M., Elliott, H. A., Randol, B., Schwadron, N. A., Sokol, J. M., Szalay, J. R., Olkin, C., Spencer, J., Stern, A., & Weaver, H. (2017), Interstellar Pickup Ion Observations to 38au. *The Astrophys. J. Supp. Ser.,* 233(8), 14. doi:https://doi.org/10.3847/1538-4365/aa91d2

Merka, J., A. Szabo, J. A. Slavin, and M. Peredo (2005), Three-dimensional position and shape of the bow shock and their variation with upstream Mach numbers and interplanetary magnetic field orientation, J. Geophys. Res., 110, A04202, doi:10.1029/2004JA010944.

Möbius, E., & Hovestadt, D. (1985), Direct observations of He$^+$ pick-up ions of interstellar origin in the solar wind. *Nature*, 318, 426 EP.

Ogilvie, K. W., D. J. Chorney, R. J. Fitzenreiter, F. Hunsaker, J. Keller, J. Lobell, G. Miller, J. D. Scudder, E. C. Sittler Jr., R. B. Torbert, D. Bodet, G. Needell, A. J. Lazarus, J. T. Steinberg, J. H. Tappan, A. Mavretic, and E. Gergin, SWE, a comprehensive plasma instrument for the WIND spacecraft, *Space Sci. Rev, 71,* 55-77, 1995.

Oka, M., Terasawa, T., Noda, H., Saito, Y., & Mukai, T. (2002a), 'Torus' distribution of interstellar helium pickup ions: Direct observation, *Geophys. Res. Lett.* 29(12), 1612, doi:10.1029/2002GL015111

Oka, M., Terasawa, R., & Noda, H. (2002b), Acceleration of interstellar helium pickup ions at the Earth's bow shock: GEOTAIL observation. *Geophys. Res. Lett.* 29(14), 1688, doi:10.1029/2001GL014150.

Paschmann, G., & Sckopke, N. (1980), Energization of Solar Wind Ions by Reflection From the Earth's Bow shock. *J. Geophys. Res.* 85(A9), 4689-4693.

Pesses, M. E., J. R. Jokipii, & D. Eichler, Cosmic Ray Drift, Shock Wave Acceleration, and the Anomalous Component of Cosmic Rays, *Astrophys. J. Lett.*, 246, L85 (1981a).

Pesses, M. E. (1981b), On the Conservation of the First Adiabatic Invariant in Perpendicular Shocks, *J. Geophys. Res.,*86, A1, 150-152, doi :10.1029/JA086iA01p00150

Pollock, C., Moore, T., Jacques, A. *et al.* Fast Plasma Investigation for Magnetospheric Multiscale. *Space Sci Rev* **199**, 331–406 (2016). https://doi.org/10.1007/s11214-016- 0245-4

Russell, C.T., Anderson, B.J., Baumjohann, W., *et al.*, 2016, *Space Sci Rev* **199**, 189–256. https://doi.org/10.1007/s11214-014-0057-3

Schwartz, S. J., P. W. Daly, and A. N. Fazakerley (1998), Spacecraft Analysis of Plasma Kinetics, in 610 Analysis Methods for Multi-Spacecraft Data (eds. G. Paschmann and P. W. Daly), ISSI Scientific 611 Reports Series, ESA/ISSI, 159-18.

Sckopke, N., & Paschmann, G. (1983), Evolution of Ion Distributions Across the Nearly Perpendicular Bow Shock: Specularly and Non-Specularly Reflected-Gyrating Ions. *J. Geophys. Res.* 88(A8), 6121-6136.

Sckopke, N., Paschmann, G., Brinca, A. L., Carlson, C. W., & Luhr, H. (1990), Ion Thermalization in Quasi-Perpendicular Shocks Involving Reflected Ions. *J. Geophys. Res.* 95(A5), 6337-6352.

Sckopke, N. (1995), Ion Heating at the Earth's Quasi-perpendicular Bow Shock. *Adv. Space Res.* 15(8/9), 261-269. 0273-1177(94)00106

Sonnerup, B. U. O. (1969), Acceleration of Particles Reflected at a Shock Front. *J. Geophys. Res., Space Physics* 74(5), 1301-1304.

Starkey, M. J., Fuselier, S. A., Desai, M. I., et al., 2019,*Geophys. Res. Lett.,* 46, 10,735–10,743. https://doi.org/10.1029/2019GL084198

Starkey, M., Fuselier, S. A., Desai, M. I., Schwartz, S. J., Gomez, R. G., Mukherjee, J., Cohen, I. J., & Russell, C. T. (2020). MMS Observations of Accelerated Interstellar Pickup He^{+} at an Interplanetary Shock. *Ap. J.,* 897:6, 10.

Stone, E. C., Cummings, A. C., McDonald, F. B., et al., 2005, *Science,* 309, 2017-2019, doi:10.1126/science.1117684.

Swaczyna, P., McComas, D. J., & Zirnstein, E. J. (2019), He+ Ions Comoving with the Solar Wind in the Outer Heliosphere, *Astrophys. J.,* 875, 36, doi:10.3847/1538-4357/ab1081

Yang, Z. W., Lembège, G., & Lu, Q. M. (2011), Impact of the nonstationarity of a supercritical perpendicular collisionless shock on the dynamics and energy spectra of pickup ions, *J. Geophys. Res.,* 116, A08216, doi:10.1029/2010JA016360.

Young, D. T., Burch, J. L., Gomez, R. G., De Los Santos, A., Miller, G. P., Wilson IV, P., Paschalidis, N., Fuselier, S. A., Pickens, K., Hertzberg, E., Pollock, C. J., Scherrer, J., Wood, P. B., Donald, E. T., Aaron, D., Furman, J., George, D., Gurnee, R. S., Hourani, R. S., Jacques, A., Johnson, T., Orr, T., Pan, K. S., Persyn, S., Pope, S., Roberts, J., Sotkes, M. R., Trattner, K. J., & Webster, J. M. (2014), Hot Plasma Composition Analyzer for the Magnetospheric Multiscale Mission. *Space Sci. Rev.* 199, 407-470. doi:10.1007/s11214-014-0119-6

Zank, G. P., Pauls, H. L., Cairns, I. H., & Webb, G. M. (1996), Interstellar pickup ions and quasi-perpendicular shocks: Implications for the termination shock and interplanetary shocks, *J. Geophys. Res.*, 101(A1), 457-477.

Zirnstein, E. J., McComas, D. J., Kumar, R., Elliott, H A., Szalay, J. R., Olkin, C. B., Spencer, J., Stern, S. A., &Young, L. A. (2018), *In Situ* Observations of Preferential Pickup Ion Heating at an Interplanetary Shock. *Phys. Rev. Lett.*, 121, 075102.